Original Paper

Eletrônica de Potência
Open Journal of Power Electronics

Received October 01, 2025; Received in revised form December 29, 2025; Accepted January 28, 2026; Date of publication February 20, 2026.
The review of this paper was arranged by Associate Editor Jéssika M. de Andrade and Editor-in-Chief Allan F. Cupertino.
Digital Object Identifier http://doi.org/10.18618/REP.e202613

Adaptive Control Based on Virtual Plant Applied to Synchronous Buck Converter using LCL Filter for Charging Lithium-Ion Batteries

Vinícius D. Rodrigues [1,*], Maicon de Miranda [1], Wagner B. da Silveira [1], Jonas R. Tibola [1], Lucas G. Scherer [1], Rodrigo V. Tambara [1]

[1]Federal University of Santa Maria - UFSM, Group of Power Electronics and Control - GEPOC, Santa Maria, RS, Brazil.

e-mail: vincius-descovi-rodrigues@ufsm.br*; maicondemiranda@hotmail.com; wagner.silveira@acad.ufsm.br; jrtibola@ctism.ufsm.br; lgscherer@gmail.com; rodvarella10@gmail.com.
*Corresponding author.

ABSTRACT

This paper introduces a virtual plant method as the main contribution, applied independently to two discrete-time adaptive control strategies for a synchronous buck converter used in battery charging: an Adaptive PI Controller (API) and a Model Reference Adaptive Controller (MRAC). The system employs an LCL filter that interfaces the power converter with the batteries. The proposed virtual plant method enhances the transient performance of adaptive systems by pre-tuning the controller gains before the physical connection, enabling automatic gain initialization and mitigating the poor start-up dynamics typical of adaptive control. The API controller performs real-time adaptation of the parameters K_p and K_i, while the MRAC is based on a reduced-order reference model to simplify its design, updating three parameters: θ_r, θ_y and θ_{vb}. A simplified methodology for designing adaptive controllers is proposed, involving plant simplification and the use of a virtual plant to automate the controller design process. Controller Hardware-in-the-Loop (C-HIL) and experimental results are presented to validate the control approaches. A fixed PI controller is used as a benchmark for comparison with the adaptive control techniques. Quantitative and qualitative analyses are provided using performance indices such as ISE, IAE, ITSE and ITAE.

KEYWORDS Adaptive Control, LCL Filter, Virtual Plant, C-HIL.

Nomenclature

α_i, β_i	Continuous plant coefficients
$\mathbf{\Gamma}$	Diagonal adaptation gain matrix of the API controller
$\boldsymbol{\omega}$	MRAC input signal vector: $\boldsymbol{\omega} = [y, r, V_b]^T$
$\boldsymbol{\theta}$	Adaptive gain vector of the MRAC controller
$\boldsymbol{\varphi}$	Error vector of the API controller: $\boldsymbol{\varphi} = [e, \sum e]^T$
$\boldsymbol{\zeta}$	Filtered input vector used for MRAC adaptation
$\boldsymbol{K}$	Adaptive gain vector of the API controller
γ	Adaptation gain of the MRAC
γ_p, γ_i	Adaptation gain of the API
$\mu\Delta_\alpha(s)$	Additive neglected dynamics in reduced-order model
ω_c^*	Desired crossover frequency (PI design)
ϕ^*	Desired phase compensation in PI design
ϖ	Discrete zero of the PI controller
a_i, δ_i	Discrete plant $G_1(z)$ coefficients
a_i, ϵ_i	Discrete plant $G_2(z)$ coefficients
a_m,b_m	Coefficients of the reference model
e	Tracking error for API and PI controller: $e = y_m - y$
e_1	Tracking error in MRAC: $e_1 = y - y_m$
G_0	Reduced-order plant model
G_1	Nominal plant model
G_2	Transfer function from battery voltage to inductor current
i_{L2}	Battery-side inductor current
k_p	Discrete proportional gain in PI design
K_p, K_i	Adaptive proportional and integral gains
m^2	Normalizer signal used in MRAC controller
m_p^2	Normalizer signal used in API controller
PM^*	Desired phase margin (PI design)
r	Reference signal
s	Laplace variable
T_s	Sampling period
u	Control signal applied to the converter
u_M	MRAC control signal
u_{API}	Control signal from the adaptive PI controller
u_{PI}	Control signal from the PI controller
V_b	Battery voltage
$W_m(s)$	Reference model transfer function
y	System output
y_m	Model reference output
y_v	Virtual plant output
z	Discrete-time complex variable

ZOH	Zero-order hold operator
API	Adaptive Proporcional Integral controller
C-HIL	Controller Hardware-in-the-Loop
HIL	Hardware-in-the-Loop
IAE	Integral of Absolute Error
ISE	Integral of Squared Error
ITAE	Integral of Time-weighted Absolute Error
ITSE	Integral of Time-weighted Squared Error
MRAC	Model Reference Adaptive Controller
SISO	Single Input Single Output

I. INTRODUCTION

The global energy transition is transforming the way we generate, store, and consume energy, driven by the urgent need to reduce carbon emissions and integrate renewable energy sources [1]. At the center of this transformation lies the critical role of energy storage technologies [2], such as lithium-ion batteries and battery energy storage systems (BESS). Lithium-ion technology offers high energy density, efficiency, and a long cycle life, which makes it essential for electric vehicles (EVs), portable electronics, and large-scale energy storage applications [3]. BESS, in particular, helps stabilize power grids by balancing supply and demand, storing excess renewable energy, and providing backup power during peak demand or outages [4].

Renewable energy generation is increasingly adopted as a sustainable alternative to conventional sources; however, its output is inherently intermittent due to environmental variability, leading to power and voltage fluctuations that compromise stability and power quality [5]. To ensure reliable operation, power electronic converters are used to regulate the generated voltage, interface with the electrical network, and coordinate the operation of energy storage systems. These storage units absorb surplus energy during periods of high generation and release it when production declines, but this process requires precise control of charging and discharging stages to maintain safe voltage levels and extend system lifespan. Consequently, the effective integration of renewable sources, energy storage technologies, and converter control strategies is essential to mitigate generation variability, improve energy efficiency, and enhance the resilience of both grid-connected and hybrid power systems [6].

Adaptive control is an advanced control strategy that dynamically adjusts the gains in real-time to optimize system performance under varying conditions. Unlike traditional fixed-gain controllers, adaptive controllers such as MRAC and API continuously monitor system behavior and modify their parameters to account for changes in system dynamics, disturbances, or uncertainties [7]–[9]. This adaptability enhances stability, responsiveness, and robustness, making it particularly useful in applications where system characteristics change over time, such as power electronics in microgrid applications [10], and renewable energies [11]. Techniques for adaptation can include model-based approaches, machine learning, or rule-based tuning methods, ensuring the controller maintains optimal performance without requiring manual retuning.

Considering the vital role that DC-DC converters play in these various applications, especially in renewable energy systems [12], robust control strategies are important to guarantee the effective and reliable functioning of these converters. To maximize energy conversion, maintain the durability and safety of components, and manage the dynamic and variable characteristics of renewable energy sources, effective control techniques are required [13], [14]. This work investigates a virtual plant–based initialization method for adaptive controllers applied to a DC battery charger with an LCL filter. The API and MRAC controllers are used only as representative adaptive strategies to demonstrate the applicability of the proposed method, which focuses on principles independent of the specific control law.

Furthermore, one of the classic problems of adaptive controllers is the gain start-up in transients. Although the gains are adapting, the start-up transient response is poor. In order to mitigate this classic problem, the virtual plant method is proposed to improve the start-up transient response, adapting the gains before the physical connection with the real plant. In [15], the virtual plant approach was evaluated only in offline PSIM simulations and exclusively with an MRAC controller. In contrast, the present work extends the methodology to real-time validation using both C-HIL and a physical prototype implemented on a low-cost STM32 microcontroller. In addition, an API controller is included to demonstrate the applicability of the virtual plant method to different adaptive strategies, and a fixed-gain PI controller is incorporated as a benchmark.

This paper proposes a virtual plant method for two independent discrete-time adaptive control techniques applied to a synchronous buck converter for charging batteries: API and MRAC controllers. The system uses an LCL filter that interfaces the power converter and the batteries. A passive damping method with a series resistor is used to attenuate the filter resonance peak. The virtual plant method is motivated by the need for a better start-up transient response of adaptive controllers; the virtual plant emulates the real plant and runs on a microcontroller, similarly to an embedded Hardware-in-the-Loop (HIL) device. The API controller uses a Gradient Descent method to adapt the controller gains K_p and K_i. The plant model reference utilizes a reduced order, with a first-order transfer function to simplify the MRAC controller project. Simple design procedures will be presented to guide the reader.

The experimental results based on C-HIL and physical prototype are presented to validate the control project and the effectiveness of the virtual plant. A fixed-gain PI controller is used as a benchmark for comparison with the adaptive control techniques. To evaluate the controllers, analyses are provided using performance indices such as ISE and IAE, which evaluate the overall tracking performance of

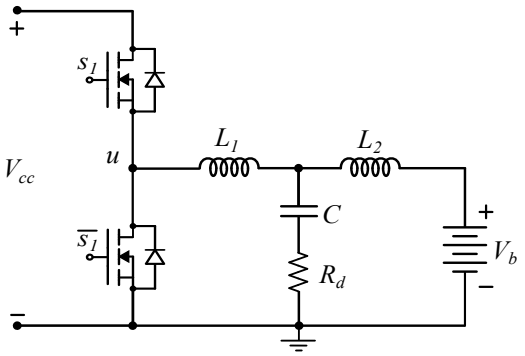

FIGURE 1. Synchronous Buck converter, LCL filter and battery

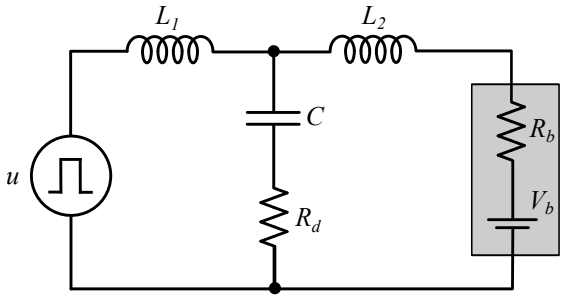

FIGURE 2. Equivalent circuit of the converter, LCL filter and battery model

the system, as well as ITSE and ITAE, which evaluate the controller with more weight in steady state [16]. The converter system was tested in two separate simulations: one using the Adaptive PI controller and another using the MRAC. Each controller was tested independently under the same reference and load conditions, allowing a fair comparison of performance. The virtual plant method was applied similarly in both adaptive control strategies.

The structure of this paper is as follows: Section II introduces the power converter and plant modeling, Section III presents the control methodology, with API and MRAC, Section IV presents the results with C-HIL, Section V presents the experimental results, and Section VI provides an overview and analysis of the results.

II. POWER CONVERTER AND PLANT

The topology used in this work is a half-bridge converter, which functions like a synchronous Buck converter. As shown in Figure 1, the power converter is fed by an external DC voltage Bus, and an LCL filter is used to make the connection between the converter and the batteries.

The LCL filter is commonly applied for grid-connected inverters, for attenuation of current harmonic components. This is a third-order filter, in comparison with a first-order filter, such as the L filter, that presents better attenuation of the harmonics provided by the switching frequency [17], [18]. The LCL filter has an attenuation of 60 dB/dec., while the L filter has 20 dB/dec., despite the more complex topology, the LCL filter can be constructed with less volume of reactive components [19], [20]. In battery charging applications, substituting an L-type filter with an LCL filter results in a charger with a compact size and lower ripple charging current. By achieving low ripple current charging is vital for battery health, as it reduces heat generated by the ripple current, thereby helping to lengthen the battery's lifetime [21], [22].

However, the LCL filter has a peak of resonance that can make the closed-loop control difficult [23]. There are two main ways to mitigate the resonance problem: passive damping and active damping. The passive damping methods use a passive damping resistor or a combination of more passive components [24], this is a good straightforward solution, but the project of the damping resistor is crucial for minimizing losses and providing the resonance peak attenuation [25]. The active damping methods include single or multi-loops methods, which use digital filters and feedback loops [26] [27], that require complex control techniques and can elevate the computational cost.

In this application, the LCL filter interfaces the power converter with the battery bank. Passive damping is adopted by inserting a resistor R_d in series with the capacitor C, as it provides a simple and reliable solution for mitigating the resonance peak in a SISO system without requiring additional sensors or control loops. Given the low-power level of the converter, the losses associated with the damping resistor are limited and acceptable for the application ($\approx$ 150 mW). This design choice does not constrain the adaptive control design, as the proposed strategies can be applied to converters employing other filter configurations. Figure 2 presents the equivalent circuit, considering the converter applies a mean voltage based on the action of control u, and the battery model is based on a zero-order internal resistance and a voltage source. The nominal voltage of a lithium-ion battery cell is 3.7 V, and the battery bank is composed of 4 battery cells in series.

For battery charging current control, the L_2 current (battery current) was chosen as the control variable. The transfer function $G_1(s)$ relates the L_2 current with the voltage control action u, which is given by (1), the coefficients of numerator β and denominator α are obtained by applying the theory of electrical circuits in the equivalent circuit presented in Figure 2, the contribution of the battery resistance R_b is considered, and the battery voltage V_b is zero.

$$G_1(s) = \frac{i_{L_2}(s)}{u(s)} = \frac{\beta_1 s + \beta_0}{\alpha_3 s^3 + \alpha_2 s^2 + \alpha_1 s + \alpha_0} \tag{1}$$

where the coefficients β and α are:

- $\beta_1 = R_d C$;
- $\beta_0 = 1$;
- $\alpha_3 = L_1 L_2 C$;
- $\alpha_2 = L_1 R_d C + L_1 R_b C + L_2 R_d C$;
- $\alpha_1 = L_1 + C R_d R_b + L_2$;
- $\alpha_0 = R_b$.

The project of the converter and damping resistor is proposed in [28], which the key equations are included in Appendix A, the Table 1 presents the values of the plant.

TABLE 1. Parameters of power converter and plant

Description	Variable	Value
Maximum battery voltage	$V_{b,\max}$	16.8 V
Nominal battery voltage	V_b	14.8 V
Minimum battery voltage	$V_{b,\min}$	10 V
Maximum charge current	$I_{b,\max}$	2.6 A
DC BUS Voltage	V_{cc}	24 V
Converter side Inductor	L_1	60 μH
Battery side Inductor	L_2	20 μH
Filter Capacitor	C	86 μF
Damping Resistor	R_d	0.5 Ω
Internal battery resistance	R_b	100 mΩ
Switching Frequency	f_{sw}	50 kHz

A. The Virtual Plant Method

The use of a virtual plant method is motivated by a better starting condition for the adaptive controller [15], [29]. It is considered that the parameters of the plant are known. For the modeling of the plant considering the disturbance of the battery voltage, the transfer function is very similar to (1), though the coefficient β_2 is included, the transfer function $G_2(s)$ that relates the L_2 current and the battery voltage V_b (2). The contribution of the power converter through the control action u is considered zero. This contribution is important for the virtual plant method because it models an external force, which is the battery voltage.

$$G_2(s)=\frac{i_{L_2}(s)}{V_b(s)}=\frac{-\beta_2 s^2-\beta_1 s-\beta_0}{\alpha_3 s^3+\alpha_2 s^2+\alpha_1 s+\alpha_0} \tag{2}$$

where the coefficients β and α are identical as shown in (1), except by $\beta_2 = L_1C$.

With the zero-order battery model, the transfer function remains third order, and the virtual plant has a good correspondence with the physical system, as can be confirmed with the simulations and experimental results. More complex battery models can be used, and the virtual plant method would remain valid as it would increase the correspondence with the physical plant, however, it would increase the order of the transfer function.

The combined contribution of the transfer functions (1) and (2), as expressed in (3), results in the current model $i_{L_2}(s)$ through the principle of superposition.

$$i_{L_2}(s) = G_1(s)u(s) + G_2(s)V_b(s) \tag{3}$$

After discretization, this model is implemented in the microcontroller as a virtual plant, which is executed before connecting the controller to the physical system. That allows the adaptive controller to operate in a simulated environment during the initialization phase, similarly to a HIL device, enabling its gains to be automatically tuned before the real converter is energized. As a result, the well-known poor start-up transient of adaptive controllers is avoided, since the control action applied to the real converter begins with adequately tuned parameters rather than zero or arbitrary initial values.

1) Discretization Method with the Z-transform

For the discrete-time model of the plant, the Z-transform is applied, considering that the average voltage of the converter is kept constant between sampling events. This is modeled as a ZOH (Zero Order Hold), as shown in (4).

$$G_z(z) = \mathcal{Z}\left\{\frac{1-e^{-sT_s}}{s}G_s(s)\right\} \tag{4}$$

The transfer function $G_1(z)$, shown in (5), represents the discrete nominal plant using symbolic coefficients. It relates the current i_{L_2}, denoted as y_1, to the control input u, and corresponds to the continuous-time model given in (1). The numerical values and the derivation of the discrete models are presented in Appendix B.

$$G_1(z)=\frac{y_1(z)}{u(z)}=\frac{\delta_2 z^2+\delta_1 z-\delta_0}{a_3 z^3-a_2 z^2+a_1 z-a_0} \tag{5}$$

The discrete model $G_2(z)$ with symbolic coefficients is shown in (6). This transfer function relates the inductor current i_{L_2}, denoted as y_2, to the battery voltage V_b, and corresponds to the continuous-time model in (2). The denominator coefficients of $G_1(z)$ and $G_2(z)$ are identical and represented by the symbols a_0, a_1, a_2 and a_3. The battery voltage V_b is applied to the plant continuously; despite this, the ZOH method was used for discretization without incurring performance penalties.

$$G_2(z)=\frac{y_2(z)}{V_b(z)}=\frac{-\epsilon_2 z^2+\epsilon_1 z-\epsilon_0}{a_3 z^3-a_2 z^2+a_1 z-a_0} \tag{6}$$

Applying the cross product in (5) and (6) makes it possible to obtain the computable recurrence equation (7), that corresponds with the continuous model (3).

$$\begin{aligned} i_{L_2}(k) = V_{cc}\Big(\sum_{i=0}^{3}\delta_i u(k-i)\Big) - \sum_{i=1}^{3} a_i y_1(k-i) \\ + \sum_{i=0}^{3}\epsilon_i V_b(k-i) - \sum_{i=1}^{3} a_i y_2(k-i) \end{aligned} \tag{7}$$

The virtual plant in (7) reproduces the behavior of the physical plant; however, the DC bus voltage V_{cc} and battery voltage V_b are real measured signals that are injected into the virtual model.

III. ADAPTIVE CONTROL METHODOLOGY

Two adaptive control schemes are presented in this section in order to regulate the battery current. The main advantage

of these approaches is their adaptive behavior. Thus, the controller gains are designed and updated automatically. Additionally, a benchmark based on a fixed-gain PI controller is presented for comparison purposes.

A. MRAC Control

The MRAC strategy aims to design an adaptive control system capable of making the plant output track the response of a predefined reference model. In this work, the plant $G_0(s)$ is considered as a first-order approximation that represents the relation between the control input $U(s)$ and the output $Y(s)$.

1) Reduction of the Plant Order

To reduce computational effort and facilitate the MRAC design, the plant was modeled as (8), where $G_0(s)$ is the reduced model of the plant and $\mu\Delta_\alpha(s)$ is an additive dynamic [30].

$$G_1(s) = G_0(s) + \mu\Delta_\alpha(s) \tag{8}$$

The part of the order reduction $G_0(s)$ is modeled as a first-order transfer function, and was obtained considering that the capacitance C is sufficiently small, the result is the transfer function present in (9), which corresponds to the real pole of the plant. The pair of conjugate complex poles is present in the non-modeled additive dynamic $\mu\Delta_\alpha(s)$. The discrete model of $G_0(s)$, using ZOH method, is present in (10).

$$G_0(s) = \frac{\frac{1}{L_1+L_2}}{s + \frac{R_b}{L_1+L_2}} \tag{9}$$

$$G_0(z) = \frac{i_{L_2}(z)}{u(z)} = \frac{0.2469}{z - 0.9753} \tag{10}$$

As shown in Figure 3, the nominal plant $G_1(z)$ and the reduced order plant $G_0(z)$ are similar at low frequencies, $G_1^*(z)$ is the same as $G_1(z)$ but with $R_d = 1\ m\Omega$, and $G_1(z)$ have passive damping by the resistor R_d as noted in Table 1, which mitigates the resonance peak of the filter.

2) Design of MRAC

To ensure that the plant exhibits the desired behavior, we define a first-order reference model, as presented in (11) [31], in this application the reference model was chosen with a real pole in 1000 rad/s. This frequency was chosen taking into consideration that the reference signal is filtered by the reference model, therefore, as the reference for battery charging is constant and with slow dynamics, the poles and zeros of the reference model may have slower dynamics as well.

$$W_m(s) = \frac{Y_m(s)}{R(s)} = \frac{b_m}{s + a_m} \tag{11}$$

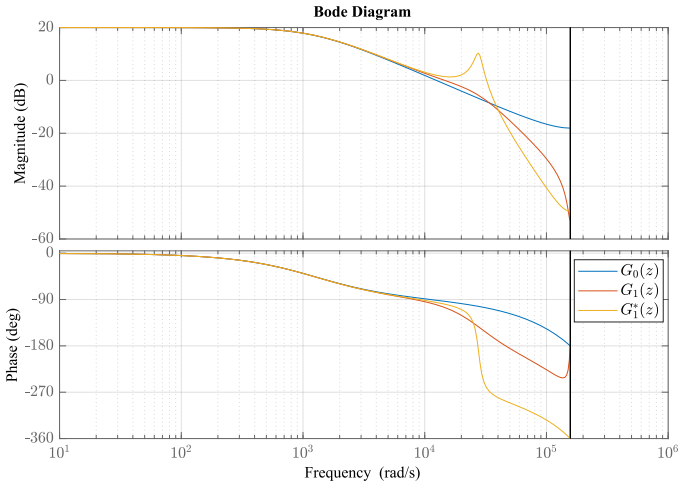

FIGURE 3. Bode diagram of nominal plant $G_1(z)$ with R_d = 0.5 Ω, $G_1^*(z)$ with R_d = 1 $m\Omega$, and reduced plant $G_0(z)$.

where $Y_m(s)$ is the desired output of the reference model in response to the input $R(s)$, b_m and a_m are respectively the numerator and denominator coefficients of the reference model.

By applying the inverse Laplace transform to the reference model, the corresponding time-domain differential equation is obtained, as shown in (12).

$$\dot{y}_m(t) = -a_m y_m(t) + b_m r(t) \tag{12}$$

The control equation is provided in (13):

$$u_M(t) = \theta_r(t)r(t) + \theta_y(t)y(t) + \theta_{V_b}(t)V_b(t) \tag{13}$$

where $\theta_r(t)$, $\theta_y(t)$, and $\theta_{V_b}(t)$ are adaptive parameters that are dynamically adjusted to minimize the tracking error. The error equation is presented in (14).

$$e_1(t) = y(t) - y_m(t) \tag{14}$$

The control action is expressed as:

$$u_M(t) = \theta^T(t)\omega(t) \tag{15}$$

where $\boldsymbol{\omega} = \begin{bmatrix} y & r & V_b \end{bmatrix}^T$ includes plant output, reference, and battery voltage disturbance. The gain vector $\boldsymbol{\theta}$ is given by $\boldsymbol{\theta} = \begin{bmatrix} \theta_y & \theta_r & \theta_{V_b} \end{bmatrix}^T$. The components V_b and θ_{V_b} are related to the battery voltage disturbance component.

3) Discrete-time Adaptive Law

The discrete-time adaptive law, descendant gradient type, for the actualization of control gains $\boldsymbol{\theta}$, can be expressed by (16), variables in the time domain (t) are presented in discrete time (k).

$$\boldsymbol{\theta}(k) = \boldsymbol{\theta}(k-1) - \frac{T_s\gamma e_1(k-1)\boldsymbol{\zeta}(k-1)}{m^2(k-1)} \tag{16}$$

where γ is the adaptation gain that defines the convergence speed of MRAC parameters. The signal m^2, shown in (17), is a normalization term to limit excessive parameter variations and improve robustness in the presence of large signals or disturbances.

$$m^2 = 1 + \boldsymbol{\zeta}^T \boldsymbol{\zeta} \tag{17}$$

where $\boldsymbol{\zeta}$ is a vector that contains relevant input and output signals. The vector $\boldsymbol{\zeta}$ is obtained by filtering the vector $\boldsymbol{\omega}$ through the reference model $W_m(s)$, as shown in (18). This filtering operation ensures that the adaptation law is driven by signals consistent with the desired closed-loop dynamics, improving stability and convergence properties.

$$\boldsymbol{\zeta} = W_m(s)\boldsymbol{\omega} \tag{18}$$

Figure 4 presents a simplified block diagram of the MRAC structure, considering the virtual plant.

B. API Controller

In the API controller, the control action is composed of proportional and integral terms with adaptive gains K_p and K_i (19).

$$u_{API}(t) = K_p(t)e(t) + K_i(t)\int_{t_0}^{t} e(\tau)d\tau \tag{19}$$

The API controller employs a descendant gradient algorithm that adjusts the gains proportional (K_p) and integral (K_i) (see Appendix C). The adaptation law of these gains is calculated as follows in (20) and (21).

$$\dot{K_p}(t) = \gamma_p e^2(t) \tag{20}$$

$$\dot{K_i}(t) = \gamma_i e(t)\int_{t_0}^{t} e(\tau)d\tau \tag{21}$$

where γ_p and γ_i are the adaptation gains that set the convergence rate. The error (e) equation is given in (22).

$$e(t) = y_m(t) - y(t) \tag{22}$$

where y_m is the reference signal r filtered by the reference model W_m, used as a reference in the API controller for comparison, and y is the plant output variable.

Considering $\boldsymbol{\Gamma}$ as the adaptation gain matrix, chosen positive definite, with γ_p and γ_i as shown in (23), and $\boldsymbol{\phi}$ is the error vector (24). The vector $\dot{\mathbf{K}}$ can be expressed as (25).

$$\boldsymbol{\Gamma} = \begin{bmatrix} \gamma_p & 0 \\ 0 & \gamma_i \end{bmatrix} \tag{23}$$

$$\boldsymbol{\phi}(t) = \begin{bmatrix} e(t) \\ \int e(t)dt \end{bmatrix} \tag{24}$$

$$\dot{\mathbf{K}}(t) = \begin{bmatrix} \dot{K_p}(t) \\ \dot{K_i}(t) \end{bmatrix} = \frac{\boldsymbol{\Gamma}\boldsymbol{\phi}(t)e(t)}{m_p^2(t)} \tag{25}$$

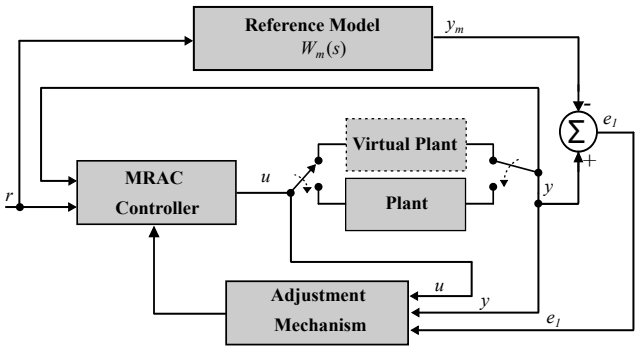

FIGURE 4. Structure of the MRAC controller with the virtual plant method.

where m_p^2 is the normalizer signal, expressed by (26), used to increase the robustness in large variations and stabilize adaptive gains in the presence of steady-state errors.

$$m_p^2(t) = 1 + y^2(t) \tag{26}$$

The discrete-time adaptive law for the API controller can be expressed by (27). Time-domain variables (t) are represented in discrete-time form using the index k.

$$\mathbf{K}(k) = \mathbf{K}(k-1) + \frac{T_s\boldsymbol{\Gamma}\boldsymbol{\phi}(k-1)e(k-1)}{m_p^2(k-1)} \tag{27}$$

Figure 5 presents a simplified block diagram of the API structure, considering the virtual plant.

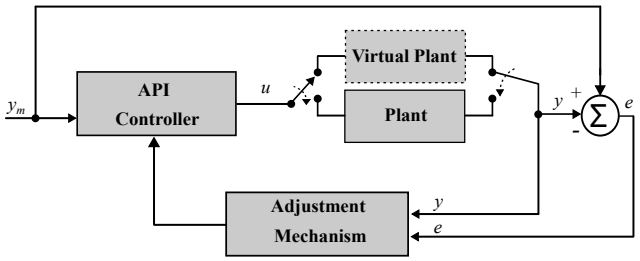

FIGURE 5. Structure of the API controller with the virtual plant method.

C. Benchmark Control Strategy

The proportional integral controller (PI) was used to perform a benchmark between control techniques, comparing adaptive control with classical control techniques. The PI controller design uses the discrete domain strategy proposed in [32]. In this strategy, the desired open-loop system crossover frequency ω_c^* and the desired phase margin PM^* are provided, and the strategy provides the proportional gain value k_p and the discrete controller zero frequency ϖ.

The method for determining the discrete controller zero frequency of the PI controller is present in (28).

$$\varpi = \frac{sin(T_s\omega_c^*) + 2\left[sin\left(\frac{T_s\omega_c^*}{2}\right)\right]^2 tan(\phi^*)}{sin(T_s\omega_c^*) - 2\left[sin\left(\frac{T_s\omega_c^*}{2}\right)\right]^2 tan(\phi^*)} \tag{28}$$

where T_s is the sampling period of the control law, and ϕ^* corresponds to the desired phase delay inserted by the controller determined by the difference between the desired phase margin (PM^*) and the phase margin measured at the desired crossover frequency, according to (29).

$$\phi^* = PM^* - \left(\pi + \angle G_1(e^{j\omega_c^* T_s})\right) \tag{29}$$

To calculate the proportional gain, an auxiliary transfer function is defined (30). Then the proportional gain is obtained considering that the gain of the open-loop transfer function must have a unitary gain at the crossover frequency, according to (31).

$$C(z) = \frac{z - \varpi}{z - 1} \tag{30}$$

$$k_p = \frac{1}{|G(e^{j\omega_c^* T_s})||C(e^{j\omega_c^* T_s})|} \tag{31}$$

With LCL filter parameters, a crossover frequency of 500 Hz, a phase margin of 60^o, and for a switching and sampling frequency of 50 kHz, k_p = 0.236 and ϖ = 0.978 were obtained. The structure of the PI controller is presented in Figure 6. The fixed gain PI control action is present in (32).

$$u_{PI}(k) = u_{PI}(k-1) + k_p e(k) - k_p \varpi e(k-1) \tag{32}$$

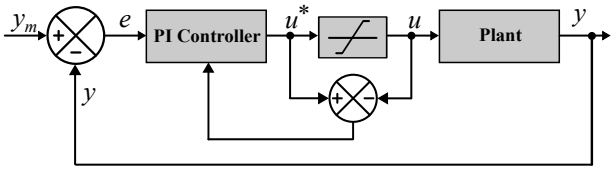

FIGURE 6. Structure of the PI controller.

IV. C-HIL RESULTS

Two independent C-HIL experiments were conducted to evaluate the adaptive control systems: one employing the Adaptive PI controller and the other using the MRAC strategy. Both controllers were separately assessed under identical reference and load conditions to ensure a fair performance comparison. The virtual plant method was applied consistently across both control approaches. To perform a benchmark between adaptive control systems and classic control strategies, results were obtained using a fixed-gain PI Controller under the same conditions employed for the adaptive controllers, allowing the generation of quantitative metrics such as ISE, ITSE, IAE, and ITAE.

Figure 7 presents the hardware setup with Typhoon HIL 402, interface board with instrumentation and signal conditioning for the microcontroller STM32H7A3ZITXQ, oscilloscope Tektronix MDO3034, and notebook. With this setup, real-time simulations were performed, and the controllers were programmed in the microcontroller.

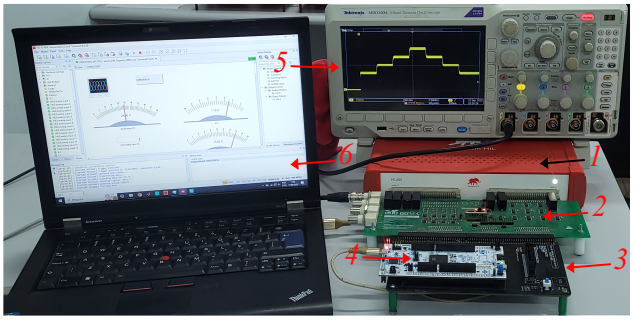

FIGURE 7. Experimental HIL setup: 1- Typhoon HIL 402; 2- Instrumentation and signal conditioning board; 3- Interface board; 4- STM32H7A3ZITXQ; 5- Oscilloscope; 6- Notebook.

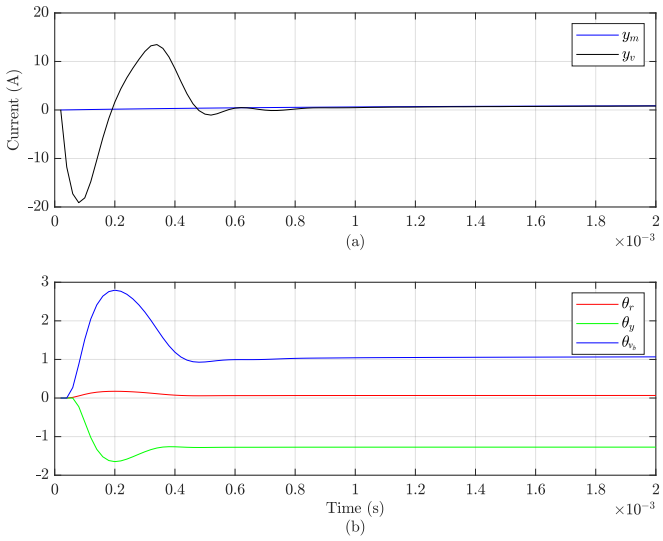

FIGURE 8. Result from microcontroller buffer: a) Initial transient response with the virtual plant (y_v) running, following the reference y_m; b) Adaptive gains θ settling time.

A. MRAC Controller

For the first result, the initial transient of the MRAC controller is presented with the adaptive parameters θ_r, θ_y, and θ_{vb} starting with null values, and the results were obtained through data saved in a microcontroller buffer. Figure 8 presents the transient where the virtual plant (y_v) is running, and the control gains $\boldsymbol{\theta}$ are adapted for the reference (y_m), the adaptation gain γ utilized was 4000, which is a hyper-parameter empirically chosen. The results show the importance of initializing the adaptive gains $\boldsymbol{\theta}$ in the system with the favored initial conditions, since the current of the virtual plant exhibits a start-up transient with a high peak of current. This peak of current during the transient will activate a protection system, making the start of the system very difficult. Figure 9 shows the C-HIL result for a start-up transient of the system without the auto-tuning gains provided by the virtual plant initialization.

The results shown in Figure 10 present a sequence of steps in the current reference. Before 0.05 s, the system runs with the virtual plant (y_v) and the gain vector $\boldsymbol{\theta}$ is tuned, in 0.05 s,

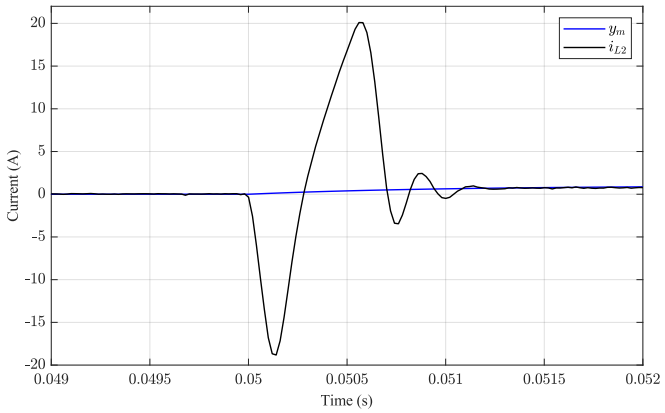

FIGURE 9. Result from microcontroller buffer: Transient response without running the virtual plant before t = 0.05 s and the connection with the real plant.

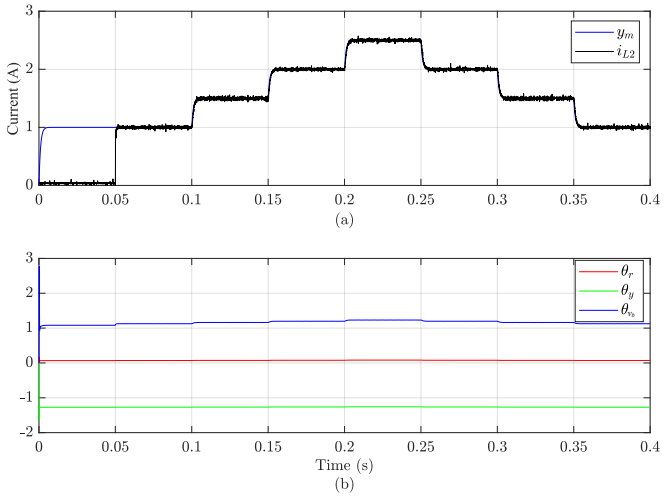

FIGURE 10. Result from microcontroller buffer: a) Real plant connection and sequence of steps in current reference; b) Adaptive gains θ.

the connection with the real plant is realized, the reference of current (y_m) was set to 1 A for both instances. It is noted that the current has a soft overshoot when the real plant (i_{L2}) is connected, because adaptive gains settle to minimize the effect for this condition of commutation. Over the reference changes, the MRAC controller performs well in tracking, and the adaptive gain θ_{V_b} explicitly changes under the steps in reference.

B. API Controller

The same experimental results were performed for the API controller. Figure 11 shows the starting transient where the virtual plant (y_v) is running, and the gains of control $\boldsymbol{K}$ are adapted for reference (y_m). The adaptation gains used were $\gamma_p = 8 \times 10^{-3}$ and $\gamma_i = 100$, which are empirically chosen, from which the gains K_p and K_i were obtained. The API controller behavior is predominantly integral, the chosen $\boldsymbol{\Gamma}$ parameter pair prioritizes low overshoot. With this matrix $\boldsymbol{\Gamma}$, the settling time of the gains K_p and K_i converges in 30 ms, slower than MRAC controller.

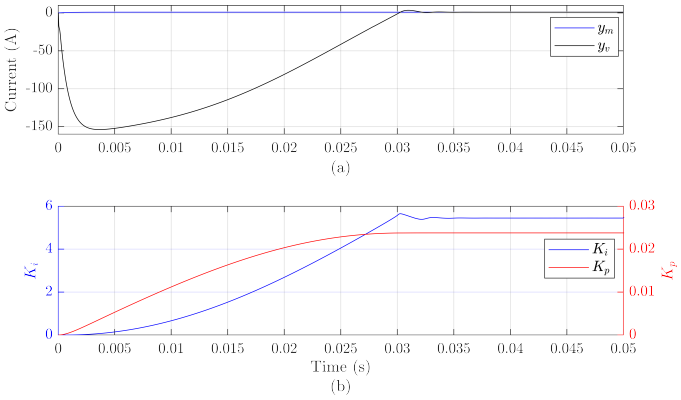

FIGURE 11. Result from microcontroller buffer: a) API controller initial transient response with the virtual plant (y_v) running, b) Adaptive gains $\boldsymbol{K}$ settling time.

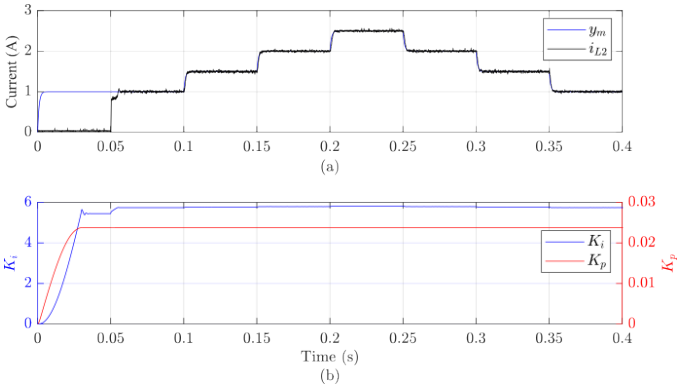

FIGURE 12. Result from microcontroller buffer: a) API controller, real plant connection and sequence of steps in the current reference; b) Adaptive gains $\boldsymbol{K}$.

The results shown in Figure 12 present a sequence of steps in the current reference. The system operates with the virtual plant (y_v), and at 0.05 s, the connection with the real plant is established, the same time utilized for the MRAC controller. The reference of current (y_m) was 1 A for both instances, the system starts with soft overshoot when the real plant (i_{L2}) is connected.

C. PI Controller

The same set of tests applied to the adaptive controllers was also carried out for the PI controller, for comparison purposes. However, the virtual plant method is not used in this case, since the PI has fixed gains that were previously calculated. Figure 13 presents a sequence of steps in the current i_{L2} reference, is the same result performed in adaptive controllers, the figure was generated with the data stored in the microcontroller buffer.

D. Comparative Analyses

In Table 2, a comparison is made on the computational effort, design effort and modeling effort between the controllers. Where H corresponds to high effort, M to medium, and L to low effort. The PI controller, which was used as a

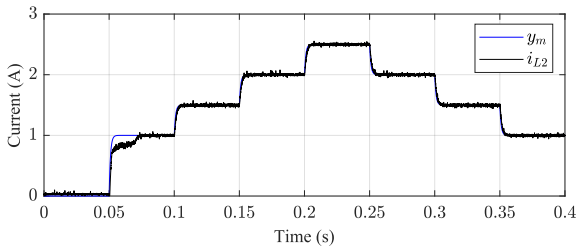

FIGURE 13. Result from microcontroller buffer: PI controller, real plant connection i_{L2} and sequence of steps in the current reference y_m.

benchmark, is considered M in design effort, whereas the point of the adaptive controllers is L, because they can perform the automatic tuning of the gains. In computational and programming efforts, the MRAC is considered H, due to the complexity, and the algorithm of adaptation is calculated in real time, which can make the implementation difficult in a microcontroller with low computational capacity. The API controller is positioned in the middle ground between the fixed-gain PI and the MRAC, it has the benefit of automatic gain design, and the computational and programming effort is lower than MRAC.

TABLE 2. Comparison Between Controllers

Controller/Index	Computational	Design effort	Programming
PI	L	M	L
API	M	L	M
MRAC	H	L	H

Quantitative metrics are presented in Table 3, to generate this index, the data stored in the microcontroller were used, as presented in Figures 10, 12 and 13, counting from the start at 50 ms to 400 ms, where the sequence of disturbances in the current reference is carried out. The results demonstrate that all controllers were able to perform reference tracking with low error. The MRAC controller performed best across all indices, followed by the API, and the fixed-gain PI controller came last. This comparison demonstrates that adaptive controllers using the virtual plant method for automatic gain design perform well, and even better than the fixed-gain PI controller.

TABLE 3. Performance metrics over current error from 50 ms to 400 ms

Index/Controller	PI	API	MRAC
IAE	10.678×10^{-3}	7.623×10^{-3}	6.072×10^{-3}
ISE	0.937×10^{-3}	0.623×10^{-3}	0.239×10^{-3}
ITAE	2.602×10^{-3}	2.022×10^{-3}	1.606×10^{-3}
ITSE	0.103×10^{-3}	0.085×10^{-3}	0.044×10^{-3}

V. Experimental Results

In order to validate the control strategies in a physical prototype, the same testing procedures were performed for the experimental results. Figure 14 shows the experimental setup, in which a low-cost STM32 microcontroller was used,

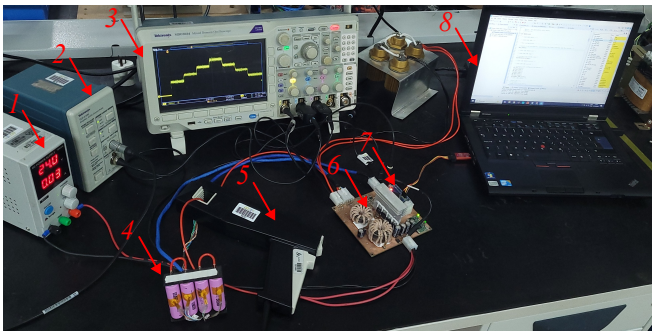

FIGURE 14. Experimental setup: 1- External power source CA-CC; 2- Current probe amplifier; 3- Oscilloscope; 4- Lithium-ion battery pack; 5- Current probe; 6- Power converter and instrumentation board; 7- STM32F407VET; 8- Notebook.

employing 4 lithium-ion batteries of the 18650 type in series, as specified in Table 1. The model of components utilized for assemble the experimental setup is presented in Table 4. The power converter, LCL filter, and instrumentation was assembled in a single board. The results are presented with oscilloscope captures and demonstrate good correspondence with the C-HIL results.

TABLE 4. Components of the experimental bench

Description	Model
CA-CC Power Source	Minipa MPS-33 30V/3A
Current probe amplifier	Tektronix TCPA 300
Oscilloscope	Tektronix MDO3034
Microcontroller	STM32F407VET
Lithium-ion battery	INR18650-26E
Mosfet	IRF4110

A. MRAC Controller

Figure 15 presents the experimental result in a physical prototype with the MRAC controller. The virtual plant method is applied for pre-tuning the adaptive gains. This result confirms that the virtual plant initialization is effective in a physical prototype even with a low-cost microcontroller.

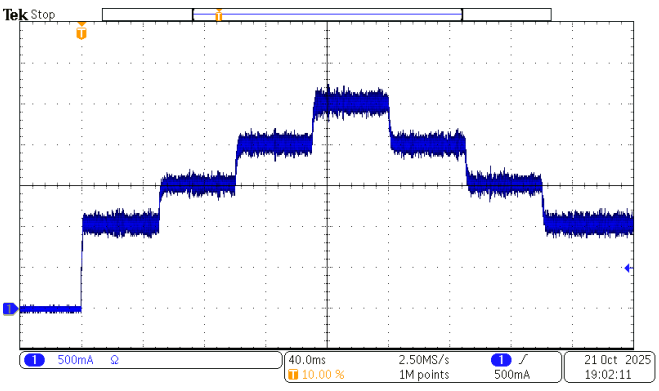

FIGURE 15. Experimental result from prototype: MRAC controller, sequence of steps in current reference.

B. API Controller

Figure 16 shows the experimental prototype results for the sequence of step changes in the current reference using the API controller. The virtual plant method is also applied, and when the physical plant (i_{L2}) is connected, the system exhibits a soft overshoot.

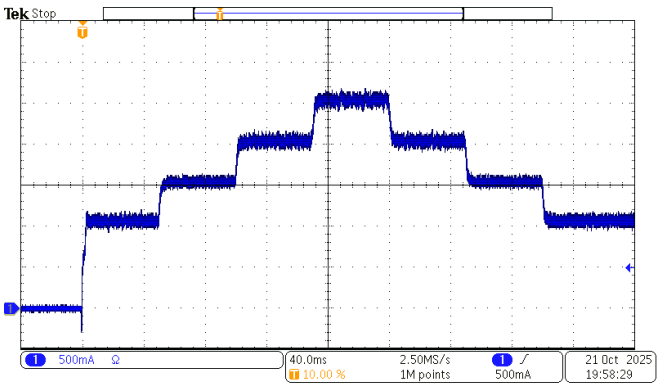

FIGURE 16. Experimental result from prototype: API controller, sequence of steps in current reference.

C. PI Controller

For comparison, the PI controller was evaluated on the physical prototype using the same test sequence applied to the adaptive controllers. In this case, the virtual plant method is not used because the PI relies on fixed, pre-computed gains. Figure 17 shows the step-response measurements of the i_{L2} current.

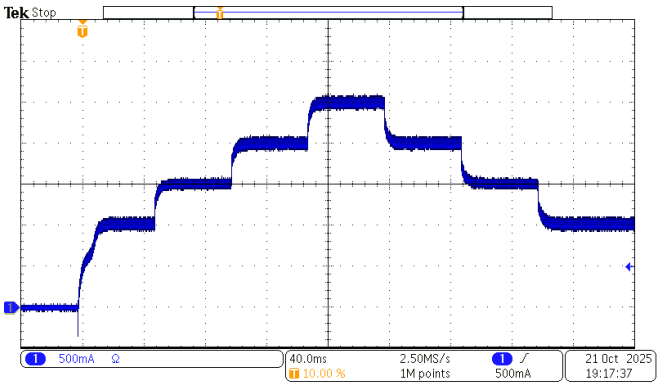

FIGURE 17. Experimental result from prototype: PI controller, sequence of steps in current reference.

VI. CONCLUSION

This paper has presented a discrete-time MRAC and API controller with a virtual plant method applied to a synchronous buck converter with LCL filter for charging batteries. The main contribution of this paper is to propose the virtual plant method to pre-tune the gains of adaptive controllers for tracking DC references with a self-tuning algorithm. This method provides a better transient response since the adaptive gains are automatically tuned before the connection with the real plant in battery-charge applications. The method is general and can be ported to other topologies of DC-DC converters and plants that use adaptive control for better starting conditions.

The adaptive controllers have a design effort advantage compared to fixed-gain controllers, since they have an automatic project independently of the plant, exhibit good stability, track the reference with low error in both transient and steady states, and are easy to implement in industry. The results show that the MRAC controller adapts its parameters significantly faster than the API controller, with a settling time below **1 ms** compared to approximately **30 ms** for the API. This settling time depends on the hyper-parameters γ. Choosing more aggressive values for γ_p and γ_i can accelerate the convergence of the adaptive gains K_p and K_i, but may also increase overshoot during the transient response. C-HIL and experimental results were presented for the validation of the method. These results indicate that virtual plant–based initialization is a practical and efficient approach for adaptive control in Li-Ion battery charging systems, with potential applications in renewable integration and electric mobility.

APPENDIX

A. LCL filter design

For the LCL filter project, first the inductor L_1 is calculated, which is based on a buck converter equation design, as shown in (33).

$$L_1 = \frac{(V_{cc} - V_{b,min})D_{min}}{f_{sw}\Delta i_{L1} i_{b,max}} \tag{33}$$

where D_{min} is the minimum duty cycle considering the minimum battery voltage $V_{b,min}$, Δi_{L1} is the maximum current variation admitted in the L_1 inductor, here is defined Δi_{L1} = 25 %. In sequence, the maximum ripple in i_{L2} is defined, Δi_{L2} = 2 %.

The ratio between i_{L2} and i_{L1} is present in (34), and with the absolute value of this transfer function in the switching frequency f_{sw} is defined a attenuation reference gain K_a^* = 0.08, as shown in (35).

$$G_{i_{L2},i_{L1}}(s) = \frac{i_{L2}(s)}{i_{L1}(s)} = \frac{R_d C s + 1}{L_2 C s^2 + (R_b C + R_d C)s + 1} \tag{34}$$

$$|G_{i_{L2},i_{L1}}(2\pi f_{sw} j)| = \frac{\Delta i_{L2}}{\Delta i_{L1}} = k_a^* \tag{35}$$

Next, the damping reference coefficient (ζ^*) is defined, for sufficient attenuation of the resonance peak $\zeta^* > 0.5$. In this project, ζ^* is defined to be 0.6. The damping resistor R_d is calculated based on ζ^* and the filter parameters, as shown in (36).

$$R_d = 2\zeta\sqrt{\frac{L_1 L_2}{C(L_1+L_2)}} \tag{36}$$

The value of the inductor L_2, according to [17], can be obtained by the quotient of the inductance L_1 and a factor $k > 0$ to be determined, $L_2 = L_1/k$.

Given the parameters above, (35) and (36) must be solved simultaneously to find C and R_d from the previously defined values of L_1, L_2, k_a^*, and ζ^*. Since this system of equations is nonlinear and complex, the `fsolve()` function from *Matlab* was used. This function solves a system of equations in the form $F(x) = 0$, as shown in (37).

$$F(x) = \begin{cases} \zeta^* - \zeta = 0 \\ k_a^* - |G_{i_{L2},i_{L1}}(2\pi f_{sw} j)| = 0 \end{cases} \tag{37}$$

where $x = [C, R_d]$ are the unknowns to be calculated. The value of the inductance $L_2 = L_1/k$ must be evaluated taking into account the losses in the damping resistor.

B. Numerical Models and Discretization Details

This appendix provides numerical details complementing the plant modeling presented in Section II. For convenience, the continuous-time coefficients α and β of the transfer functions defined in (1) and (2) are presented here in numerical form using the parameters of Table 1:

- $\beta_2 = 5.16 \times 10^{-9}$;
- $\beta_1 = 4.3 \times 10^{-5}$;
- $\beta_0 = 1$;
- $\alpha_3 = 1.032 \times 10^{-13}$;
- $\alpha_2 = 3.956 \times 10^{-9}$;
- $\alpha_1 = 8.43 \times 10^{-5}$;
- $\alpha_0 = 0.1$.

The numerical coefficients in (38) and (39), corresponding to the discrete-time transfer functions (5) and (6), were obtained using the `c2dm()` command in *MATLAB* with the zero-order hold (ZOH) method, consistent with the digital implementation in the microcontroller, using a sampling period T_s = 20 μs.

$$G_1(z) = \frac{i_{L_2}(z)}{u(z)} = \frac{0.0745z^2 + 0.02037z - 0.04218}{z^3 - 2.239z^2 + 1.709z - 0.4646} \tag{38}$$

$$G_2(z) = \frac{i_{L_2}(z)}{V_b(z)} = \frac{-0.7356z^2 + 1.302z - 0.6194}{z^3 - 2.239z^2 + 1.709z - 0.4646} \tag{39}$$

C. Deduction of the API gains

In the approach used in this work, to calculate the gains K_p and K_i, the adaptive PI gains are calculated directly, without the need to explicitly estimate the plant parameters.

Thus, consider that the plant is represented by the following transfer function:

$$G(s) = k_p \frac{B(s)}{A(s)} \tag{40}$$

where $k_p \neq 0$ is the static gain, and $B(s)$ and $A(s)$ are monic polynomials. The following assumptions are made:
1. The plant is minimum-phase, meaning that $B(s)$ is a Hurwitz polynomial;
2. The system is causal and asymptotically stable;
3. The sign of k_p is known.

A PI controller is considered, defined by the following control law:

$$u(t) = \text{sign}(k_p)(u_p(t) + u_i(t)) \tag{41}$$

where sign$(\cdot)$ represents the sign function, and u_p and u_i are the proportional and integral components, respectively:

$$u_p = K_p(t)e(t) \tag{42}$$

$$u_i = K_i(t)\int_{t_0}^{t} e(\tau)d\tau \tag{43}$$

where $K_p(t)$ and $K_i(t)$ are the proportional and integral gains, which are adjusted online. The tracking error e is computed based on a constant reference y_m and the measured output y:

$$e(t) = y_m(t) - y(t) \tag{44}$$

To update the PI gains online, a cost function is defined as:

$$J = \frac{1}{2}e^2 \tag{45}$$

To minimize J, we will use a gradient descent-type adaptation law applied to the parameters K_p and K_i.

First, we compute the gradient of J with respect to the parameters K_p and K_i:

$$\frac{\partial J}{\partial K_p} = e\frac{\partial e}{\partial K_p} \tag{46}$$

$$\frac{\partial J}{\partial K_i} = e\frac{\partial e}{\partial K_i} \tag{47}$$

Since y_m is independent of the PI gains, the derivatives of the error are:

$$\frac{\partial e}{\partial K_p} = -\frac{\partial y}{\partial K_p} \tag{48}$$

$$\frac{\partial e}{\partial K_i} = -\frac{\partial y}{\partial K_i} \tag{49}$$

In order to simplify the mathematical analysis and derive implementation equations that do not depend on the detailed mathematical model of the plant, assume that the dynamics of y and u are similar, that the plant $G(s)$ has unit DC gain, and that the control gains K_p and K_i vary slowly. Thus:

$$\frac{\partial y}{\partial K_p} \approx \frac{\partial u}{\partial K_p} \tag{50}$$

$$\frac{\partial y}{\partial K_i} \approx \frac{\partial u}{\partial K_i} \tag{51}$$

Additionally, assume that the proportional and integral control actions are independent. Then, we can write:

$$\frac{\partial y}{\partial K_p} \approx \frac{\partial u_p}{\partial K_p} \tag{52}$$

$$\frac{\partial y}{\partial K_i} \approx \frac{\partial u_i}{\partial K_i} \tag{53}$$

Hence, the gradients become:

$$\frac{\partial J}{\partial K_p} \approx -\frac{\partial u_p}{\partial K_p} = -e^2 \tag{54}$$

$$\frac{\partial J}{\partial K_i} \approx -\frac{\partial u_i}{\partial K_i} = -e \int_{t_0}^{t} e(\tau) d\tau \tag{55}$$

This yields the following adaptation laws (based on MIT Rules) for the gains:

$$\dot{K_p} = -\gamma_p \frac{\partial J}{\partial K_p} = \gamma_p e^2 \tag{56}$$

$$\dot{K_i} = -\gamma_i \frac{\partial J}{\partial K_i} = \gamma_i e \int_{t_0}^{t} e(\tau) d\tau \tag{57}$$

where γ_p and γ_i are the learning rates for the proportional and integral actions, respectively.

ACKNOWLEDGMENT

This work was financially supported in part by the funding agencies CNPq grant 308082/2025-7 and CAPES/PROEX Financing code 001.

AUTHOR'S CONTRIBUTIONS

V.D.RODRIGUES: Conceptualization, Data Curation, Formal Analysis, Investigation, Methodology, Software, Validation, Writing – Original Draft, Writing – Review & Editing. **M.D.MIRANDA:** Investigation, Software, Visualization, Writing – Review & Editing. **W.B.D.SILVEIRA:** Investigation, Software, Visualization, Writing – Review & Editing. **J.R.TIBOLA:** Data Curation, Formal Analysis, Supervision, Writing – Original Draft, Writing – Review & Editing. **L.G.SCHERER:** Data Curation, Formal Analysis, Supervision, Writing – Original Draft, Writing – Review & Editing. **R.V.TAMBARA:** Conceptualization, Data Curation, Formal Analysis, Funding Acquisition, Investigation, Validation, Writing – Original Draft, Writing – Review & Editing.

PLAGIARISM POLICY

This article was submitted to the similarity system provided by Crossref and powered by iThenticate – Similarity Check.

DATA AVAILABILITY

The data used in this research is available in the body of the document.

REFERENCES

[1] J. Qiu, J. Zhao, F. Wen, J. Zhao, C. Gao, Y. Zhou, Y. Tao, S. Lai, "Challenges and Pathways of Low-Carbon Oriented Energy Transition and Power System Planning Strategy: A Review", *IEEE Transactions on Network Science and Engineering*, vol. 11, no. 6, pp. 5396–5416, Nov. 2024, doi:10.1109/TNSE.2023.3344729.

[2] V. Sihvonen, S. Honkapuro, "The Role of Energy Storage in Promoting Sustainable Energy Transition in an Island Community", *in 2024 20th International Conference on the European Energy Market (EEM)*, pp. 1–7, Jun. 2024, doi:10.1109/EEM60825.2024.10608853.

[3] S. Bampi, G. Waltrich, A. Vaccari, "Electronic Load for Parameter Characterization in Equivalent Circuit Models of Lithium-Ion Batteries", *Eletrônica de Potência*, vol. 30, p. e202521, Feb. 2025, doi:10.18618/REP.e202521.

[4] R. C. de Barros, W. C. S. Amorim, W. d. C. Boaventura, A. F. Cupertino, V. F. Mendes, H. A. Pereira, "Methodology for BESS Design Assisted by Choice Matrix Approach", *Eletrônica de Potência*, vol. 29, p. e202412, Jun. 2024, doi:10.18618/REP.2005.1.019027.

[5] S. Ahmed, A. Ali, J. Ahmed Ansari, S. Abdul Qadir, L. Kumar, "A Comprehensive Review of Solar Photovoltaic Systems: Scope, Technologies, Applications, Progress, Challenges, and Recommendations", *IEEE Access*, vol. 13, pp. 69723–69750, Apr. 2025, doi:10.1109/ACCESS.2025.3558539.

[6] C. Sun, S. Wang, J. Pou, C. J. Gajanayake, A. K. Gupta, "Asymmetrical-Bidirectional Input-Series–Output-Parallel Modular DC–DC Converter in DC Distribution Grids With Renewables", *IEEE Transactions on Power Electronics*, vol. 39, no. 4, pp. 3943–3949, Apr. 2024, doi:10.1109/TPEL.2023.3329775.

[7] P. J. D. O. Evald, G. V. Hollweg, R. V. Tambara, H. A. Gründling, "A Discrete-Time Robust Adaptive PI Controller for Grid-Connected Voltage Source Converter with LCL Filter", *Eletrônica de Potência*, vol. 26, no. 1, p. 19–30, Mar. 2021, doi:10.18618/REP.2021.1.0053.

[8] N. Karchi, D. B. Kulkarni, "Development and analysis of adaptive PID controller using LMS algorithm for Distribution Generation-Inverter", *in 2021 Fourth International Conference on Electrical, Computer and Communication Technologies (ICECCT)*, pp. 1–7, Sep. 2021, doi:10.1109/ICECCT52121.2021.9616702.

[9] J. R. Massing, M. Stefanello, H. A. Gründling, H. Pinheiro, "Adaptive Voltage Control of Grid-Forming Inverters", *in 2023 IEEE 24th Workshop on Control and Modeling for Power Electronics (COMPEL)*, pp. 1–7, Jun. 2023, doi:10.1109/COMPEL52896.2023.10221056.

[10] B. C. Moura, P. J. dos Santos Neto, D. B. Rodrigues, C. Guimarães, L. C. G. Freitas, J. P. C. Silveira, G. B. de Lima, "Evaluating Adaptive Droop Control for Steady-State Power Balancing in DC Microgrids Using Controller Hardware-in-the-Loop", *Eletrônica de Potência*, vol. 29, p. e202451, Dec. 2024, doi:10.18618/REP.e202451.

[11] S. Swathi, B. S. Kumar, J. Upendar, "Adaptive Fuzzy-PID Droop Control VF Stabilization For Robust Renewable Micro Grid System During Grid Islanding Condition", *in 2024 IEEE 4th International Conference on Sustainable Energy and Future Electric Transportation (SEFET)*, pp. 1–6, Aug. 2024, doi:10.1109/SEFET61574.2024.10717979.

[12] F. G. Nimitti, A. M. S. S. Andrade, "Study and Design of a Non-Isolated Bidirectional DC-DC Converter Based on a Switched Inductor and Voltage Multiplier Cell for Renewable Energy Applications", *Eletrônica de Potência*, vol. 30, p. e202558, Nov. 2025, doi:10.18618/REP.e202558.

[13] M. Triggianese, H. Carbonnier, F. Tonicello, M. R. Rogina, "Two-Domains Control of a Buck Converter", *in E3S Web of Conferences*, vol. 16, p. 14005, EDP Sciences, May 2017, doi:10.1051/e3sconf/20171614005.

[14] H.-H. Chou, J.-Y. Chen, T.-H. Tseng, J.-Y. Yang, X. Yang, S.-F. Wang, "A New Control Scheme for the Buck Converter", *Applied Sciences*, vol. 13, no. 3, Feb. 2023, doi:10.3390/app13031991.

[15] V. D. Rodrigues, J. V. Merlo, J. R. Tibola, R. V. Tambara, "Adaptive Control Applied to Half-Bridge Synchronous Buck Converter using LCL Filter for Charging Batteries", *in 2024 16th Seminar on Power Electronics and Control (SEPOC)*, pp. 1–6, Oct. 2024, doi:10.1109/SEPOC63090.2024.10747481.

[16] I. S. Chaitanya, K. V. Raj, J. Ramprabhakar, R. Anand, V. P. Meena, A. Kumar, "Performance Evaluation of EHO and GWO Optimization Techniques for PI Controller Tuning of Boost Converter in Photovoltaic based Microgrid", *in 2024 2nd International Conference on*

Self Sustainable Artificial Intelligence Systems (ICSSAS), pp. 1529–1534, Oct. 2024, doi:10.1109/ICSSAS64001.2024.10760530.

[17] M. Liserre, F. Blaabjerg, S. Hansen, "Design and control of an LCL-filter-based three-phase active rectifier", *IEEE Transactions on Industry Applications*, vol. 41, no. 5, pp. 1281–1291, Oct. 2005, doi:10.1109/TIA.2005.853373.

[18] D. M. Lima, B. M. Lima, L. A. Maccari, J. E. Normey-Rico, "Kalman Filter Observers with Harmonic Disturbance Estimation Applied to a Grid-Connected LCL Filter", *in 2018 13th IEEE International Conference on Industry Applications (INDUSCON)*, pp. 730–737, Nov. 2018, doi:10.1109/INDUSCON.2018.8627294.

[19] M. Liserre, F. Blaabjerg, R. Teodorescu, "Grid Impedance Estimation via Excitation of LCL -Filter Resonance", *IEEE Transactions on Industry Applications*, vol. 43, no. 5, pp. 1401–1407, Oct. 2007, doi:10.1109/TIA.2007.904439.

[20] M. Su, B. Cheng, Y. Sun, Z. Tang, B. Guo, Y. Yang, F. Blaabjerg, H. Wang, "Single-Sensor Control of LCL-Filtered Grid-Connected Inverters", *IEEE Access*, vol. 7, pp. 38481–38494, Mar. 2019, doi:10.1109/ACCESS.2019.2906239.

[21] X. Zhou, X. Yu, S. Lukic, A. Huang, "LCL filter utilized in battery charging applications to achieve compact size and low ripple charging", *in 2012 IEEE Energy Conversion Congress and Exposition (ECCE)*, pp. 660–665, Sep. 2012, doi:10.1109/ECCE.2012.6342758.

[22] E. Şanal, P. Dost, C. Sourkounis, "LCL-Filter design for a battery charger based on buck converter (DCDC converter)", *in 2016 IEEE International Conference on Renewable Energy Research and Applications (ICRERA)*, pp. 617–621, Nov. 2016, doi:10.1109/ICRERA.2016.7884408.

[23] Y. Han, Z. Li, P. Yang, C. Wang, L. Xu, J. M. Guerrero, "Analysis and Design of Improved Weighted Average Current Control Strategy for LCL-Type Grid-Connected Inverters", *IEEE Transactions on Energy Conversion*, vol. 32, no. 3, pp. 941–952, Feb. 2017, doi:10.1109/TEC.2017.2669031.

[24] J.-Y. Lee, Y.-P. Cho, H.-S. Kim, J.-H. Jung, "Design methodology of passive damped LCL filter using current controller for grid-connected three-phase voltage-source inverters", *Journal of Power Electronics*, vol. 18, pp. 1178–1189, Jul. 2018, doi:10.6113/JPE.2018.18.4.1178.

[25] R. Peña-Alzola, M. Liserre, F. Blaabjerg, R. Sebastián, J. Dannehl, F. W. Fuchs, "Analysis of the Passive Damping Losses in LCL-Filter-Based Grid Converters", *IEEE Transactions on Power Electronics*, vol. 28, no. 6, pp. 2642–2646, Jun. 2013, doi:10.1109/TPEL.2012.2222931.

[26] L. A. Serpa, S. Ponnaluri, P. M. Barbosa, J. W. Kolar, "A Modified Direct Power Control Strategy Allowing the Connection of Three-Phase Inverters to the Grid Through LCL Filters", *IEEE Transactions on Industry Applications*, vol. 43, no. 5, pp. 1388–1400, Oct. 2007, doi:10.1109/TIA.2007.904438.

[27] W.-Y. Sung, H. M. Ahn, J.-H. Ahn, C.-Y. Oh, B. K. Lee, "Sensorless active damping method of LCL-filter in grid-connected parallel inverters for battery energy storage systems", *in 2017 IEEE 3rd International Future Energy Electronics Conference and ECCE Asia (IFEEC 2017 - ECCE Asia)*, pp. 1425–1429, Jun. 2017, doi:10.1109/IFEEC.2017.7992253.

[28] V. D. Rodrigues, A. O. Damasceno, J. R. Tibola, "Modelagem e Controle de Conversor com Filtro LCL Para Carga e Descarga de Baterias de Íons de Lítio", *in Proceedings of the 15th Seminar on Power Electronics and Control SEPOC*, Universidade Federal de Santa Maria, UFSM, Santa Maria, Oct. 2023, doi:10.53316/sepoc2023.020.

[29] W. B. da Silveira, P. J. D. d. O. Evald, A. S. Lucena, R. V. Tambara, H. A. Grundling, "Auto-Tuning of Adaptive Control Initial Gains Using Virtual System-Based Approach in Grid-Tied Converters", *Eletrônica de Potência*, vol. 30, p. e202556, Oct. 2025, doi:10.18618/REP.e202556.

[30] P. J. D. O. Evald, R. V. Tambara, H. A. Gründling, "A Direct Discrete-Time Reduced Order Robust Model Reference Adaptive Control for Grid-Tied Power Converters with Lcl Filter", *Eletrônica de Potência*, vol. 25, no. 3, p. 361–372, Sep. 2020, doi:10.18618/rep.2020.3.0039.

[31] R. Tambara, *Controle Adaptativo: Teoria e Aplicação*, Editora UFSM, 2024, URL: https://books.google.com.br/books?id=mkcAEQAAQBAJ.

[32] J. R. Tibola, R. L. Sari, T. D. M. Lanzanova, M. E. S. Martins, H. Pinheiro, "Modeling and Control of a Low-Cost Driver For an Eddy Current Dynamometer", *Journal of Control, Automation and Electrical Systems*, vol. 27, no. 4, pp. 368–378, Apr. 2016, doi:10.1007/s40313-016-0244-4.

BIOGRAPHIES

Vinícius Descovi Rodrigues received the degree in Industrial Electronics Technology from the Colégio Técnico Industrial de Santa Maria (CTISM) at the Federal University of Santa Maria (UFSM), Brazil, in 2023. He is currently pursuing the M.Sc. degree in Electrical Engineering at the Graduate Program in Electrical Engineering (PPGEE) of UFSM, in the area of applied control. Since 2015, he has been working as an Electroelectronic Technician at the Research and Development Center in Electrical Engineering (NUPEDEE) of UFSM. His research interests include power electronics, control systems, and renewable energy applications.

Maicon de Miranda received the B.Sc. and M.Sc. in Electrical Engineering at the UFSM in 2019 and 2022, respectively. Currently, he is a Ph.D. student in Electrical Engineering at UFSM, and a member of GEPOC. His main research interests include adaptive and resonant control techniques, control of distributed and grid-connected power systems, and the integration of renewable energy sources.

Wagner Barreto da Silveira received the B.Sc. and M.Sc. in Electrical Engineering at the Federal University of Santa Maria (UFSM) in 2018 and 2021, respectively. Currently, he is a Ph.D. candidate in Electrical Engineering at UFSM, and a member of the Group of Power Electronics and Control (GEPOC) of UFSM. His main topics of research are adaptive control theory, grid-connected power system control, and renewable energy systems.

Jonas Roberto Tibola was born in Tenente Portela, Brazil, 1988. He received the master's and Ph.D. degrees in electrical engineering from Federal University of Santa Maria (UFSM), Santa Maria, Brazil, in 2013 and 2017, respectively. He worked as a Lecturer with Federal Institute of Education, Venâncio Aires, Brazil, from 2015 to 2016. He is currently with UFSM, where he has been a Professor with Technical and Industrial School of Santa Maria (CTISM). He is also a Researcher with Computational Systems Research and Development Group (GSEC) and Power Electronic Research Group (GEPOC), UFSM. His research interests include modeling, control and instrumentation of pulsewidth modulation (PWM) inverters, PWM modulation strategies, and dc–dc converters.

Lucas Giuliani Scherer was born on October 8, 1983 in Santa Maria, he is an electrical engineer (2007), master (2012) and doctor in Electrical Engineering (2016) from the Federal University of Santa Maria (UFSM). He is currently an adjunct professor at UFSM. His areas of interest are: power electronics, electrical energy processing, electronic control systems, distributed generation systems and electrical machine drives. He is a member of SOBRAEP.

Rodrigo Varella Tambara received the B.Sc., M.Sc., and Ph.D. degrees in electrical engineering from the Federal University of Santa Maria (UFSM), Santa Maria, Brazil, in 2008, 2010, and 2014, respectively. He is currently an Adjunct Professor with CTISM/UFSM and a Researcher with Power Electronics and Control Group (GEPOC) and Group on Electrical and Computer Systems (GSEC). His research interests include theory and application of control systems, electronic instrumentation, and power electronics.